Finite-Source Based Stress Drop Estimates for the 2019 Ridgecrest, CA Sequence

Final Project Report

By Douglas Dreger, Jose Magana, Taka'aki Taira

Abstract

We apply a finite-source inversion method for stress drop that fits seismic moment rate functions for the distribution of fault slip, the kinematic rise time and rupture velocity parameters for aftershocks of the 2019 Ridgecrest, California earthquake. The seismic moment rate functions are derived from spectral domain deconvolution of nearby smaller earthquakes referred to as empirical Green's functions (EGF, e.g. Hartzell, 1978). The finite-source slip models are used to estimate the rupture area, the average slip, as well as the coseismic stress change (Ripperger and Mai, 2004) to determine the peak and average stress drop (e.g. Dreger et al., 2007). We have studied 7 aftershocks of the 2019 Ridgecrest earthquake sequence ranging in magnitude from 4.0 to 5.5, and we also compare the results with our published results for the Ridgecrest foreshock (Mw6.4) and mainshock (Mw7.0) (Wang et al., 2020). The results indicate self-similar scaling where the estimated rupture area is consistent with the Leonard (2010) scaling relationship within the 2-sigma uncertainty. There is variability in stress drop with both low, and high stress drop outliers. Typical finite-source analysis requires independent information on fault orientation, which can limit the utility for small magnitude events. We apply a grid search over fault strike and dip in the finite-source inversion to investigate the feasibility of using a finite-source approach on low magnitude Ridgecrest aftershocks where there may be no information about fault orientation. The results indicate that it is possible to find a best fitting orientation that is generally consistent with independent focal mechanism results. For the distribution of best fitting (>95%) models the estimated rupture area and average slip, and therefore stress drop are well resolved. The finite-source results indicate the average stress drop of the studied events is between 1-2 MPa, with a total range from 0.36 to 17.0 MPa.

Overview of EGF Selection and Deconvolution Method

The empirical Green's function method (e.g. Hartzell, 1978) is used to determine seismic moment rate functions in which the signals from a nearby smaller event is deconvolved from those for a larger target event to remove common path, site and instrument terms. Empirical Green's functions were found for specific target events by first searching event catalogs for nearby earthquakes, then performing a cross-correlation to identify those with similar waveforms and then finally applying a spectral domain deconvolution to assess if a pulse-like moment rate function is obtained. The recovery of a pulse from the deconvolution validates the empirical Green's function assumption because if the mechanisms are too different or the EGF is not located near the primary slip of the target event stable pulses are not recovered. This is an advantage of the approach in that if the empirical Green's function assumptions are not satisfied then downstream processing is not possible. EGF approaches utilizing only the spectral ratios of amplitude spectra do not have as stringent a test of the suitability of a given EGF-target event pairing.

Overview of Finite-Source Method for Stress Drop

Mori and Hartzell's (1990) method of inverting moment rate functions for fault slip, as implemented in Dreger (1997) is applied to aftershocks of the 2019 Ridgecrest earthquake. This method has proven successful in studying rupture processes of small to great earthquakes (e.g. Mori and Hartzell, 1990; Mori, 1993; Dreger, 1994; Dreger, 1997; Hough and Dreger, 1994; Dreger et al., 2007; Antolik et al., 1996, 2000). Stress drop may be estimated from the finite-source slip distribution using Ripperger and Mai (2004). This method for determining average stress drop is advantageous in that it avoids reliance on measurement of corner frequencies and the mapping of corner frequency to rupture dimension using idealized mechanical models, which have a 5.58-fold range of epistemic uncertainty (e.g. Brune, 1970; Madariaga, 1976; Sato and Hirasawa, 1973, Kaneko and Shearer, 2013). Because a kinematic finite-source model is used, azimuthal variation in observed source duration (corner frequency) due to rupture directivity is accounted for. Derived slip models even for small earthquakes are rarely the idealized circular ruptures that are employed in traditional corner-frequency-based analysis for stress drop. In addition, the finite-source method is capable of identifying the causative fault plane of the earthquake (e.g. Mori and Hartzell, 1990; Mori 1993; Dreger, 1997), as well as potentially determine the earthquake rise time and rupture velocity.

The kinematic model does require discretization of a fault plane, and the application of spatial smoothing as regularization in the inversion. For the Ridgecrest aftershocks we used a subfault dimension in the range of 0.08-0.13 km with and overall fault dimension of 5-8 km. Smoothing was optimized by using a tradeoff curve where a value of the smoothing weight was chosen to provide a smooth model with close to the maximum fit. The same smoothing was applied to all of the aftershocks studied. The model also requires the shear wave velocity and density to be specified. The shear wave velocity in concert with the rupture velocity controls the moment release from each of the subfaults. A grid search was performed over both rise time (0.04 to 0.2 seconds) and rupture velocity (~ 30% to 100% of the shear wave velocity). As described in Dreger (1997) the inversion of the moment rate functions yields a spatial model of moment release, which is then converted to slip using the specified shear wave velocity and density to define the rigidity elastic modulus. We assumed the layered velocity and density model from Wang et al. (2020) that was used in finite-source analysis of the 2019 Ridgecrest fore- and mainshocks.

The workflow for studying aftershocks of the 2019 Ridgecrest earthquake involves the selection of possible empirical Green's functions and determination of moment rate functions as described above, the testing of the two possible nodal planes from either first-motion polarity or seismic moment tensor solutions over a suite of rise time (0.04 to 0.2 seconds) and rupture velocity (1 to 3 km/s), and then finally for preferred risetime and rupture velocity values a grid search of finite-source solutions over the entire fault strike and dip space. This latter step is examined in this research to evaluate a more automated finite-source-based stress drop method that is independent of the requirement of a known focal mechanism, which would be useful in applications to smaller target earthquakes. Finally, the preferred slip distribution from the analysis is used to determine the rupture area, peak and average slip, and peak and average stress drop using Ripperger and Mai (2004).

Demonstration of Method for a Mw 4.08 event near Coso Junction (EVT7)

In this section the steps of the inversion applied to all of the Ridgecrest aftershocks are demonstrated for a Mw 4.08 event located near Coso Junction. Figure 1 shows the location of the Mw 4.1 event on July 10, 2019 at 00:48:17 UTC and nearby SCSN stations. A moment tensor solution from the SCSN is available indicating a principally strike-slip mechanism (str=232/323; dip=83/89; rake-1/=-179,; Moment=1.68e+22 dyne cm). Seismic moment rate functions with good signal to noise were obtained by spectral domain deconvolution using a nearby M 2.89 event (Figure 1). The overall duration of this earthquake is approximately 0.6 seconds.

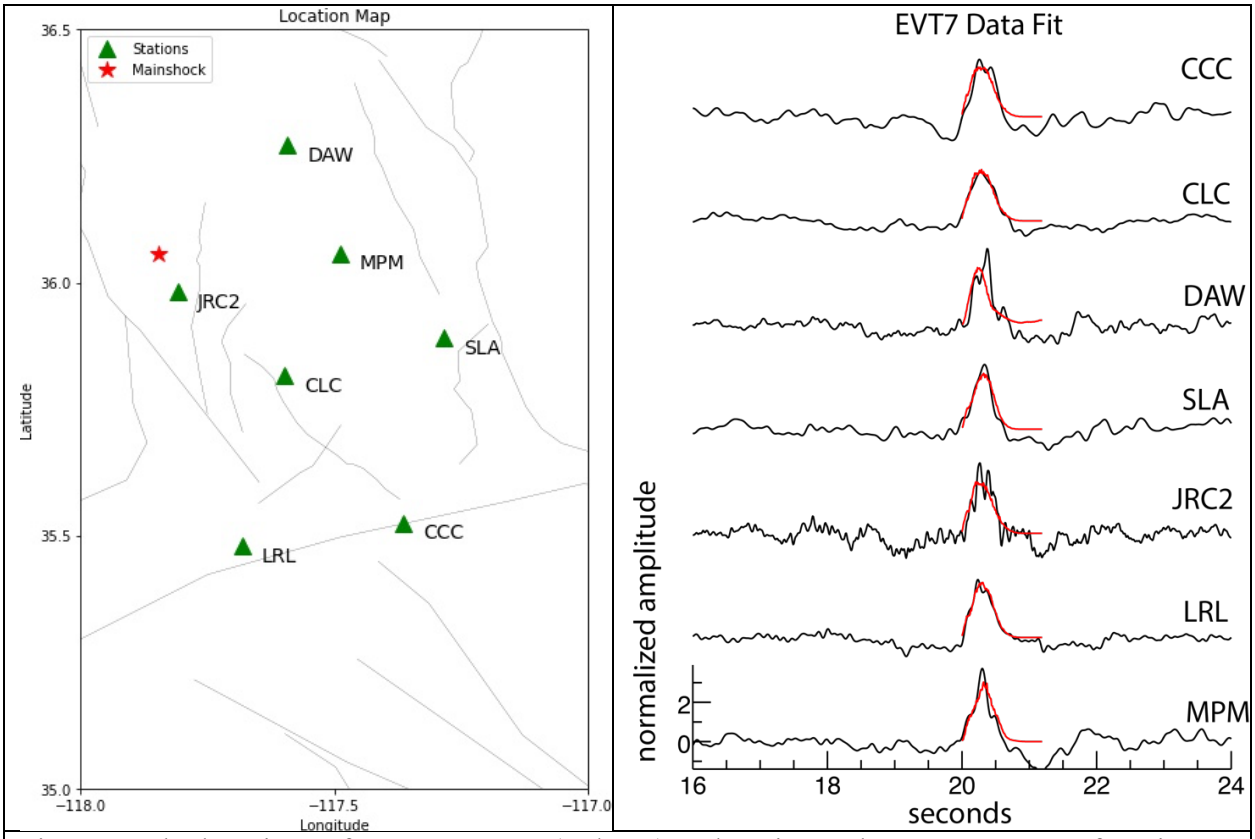

Figure 1. The locations of Mw4.08 event (red star) and stations where moment rate functions were inverted for the finite source model. The fit to observed moment rate functions (black) and synthetics (red) is shown. The amplitude of the observations is scaled by the area under the pulse between zero crossings.

A grid search performed over risetime and rupture velocity revealed that plane 2 (323/89/-173) provided a superior fit to the data (Figure 2). The results show that faster rupture velocity better fits the data and that risetime is not well determined. Considering the overall duration of 0.6 seconds we assumed a risetime of 0.06 seconds (horizontal dashed line, Figure 2) and a rupture velocity of 2.4 km/s (representing 90% of the shear wave velocity). The assumed rise time is 10% of the overall source duration to be consistent with the observations of Heaton (1990). The fit to the data for this model is good as shown by the red traces in Figure 1.

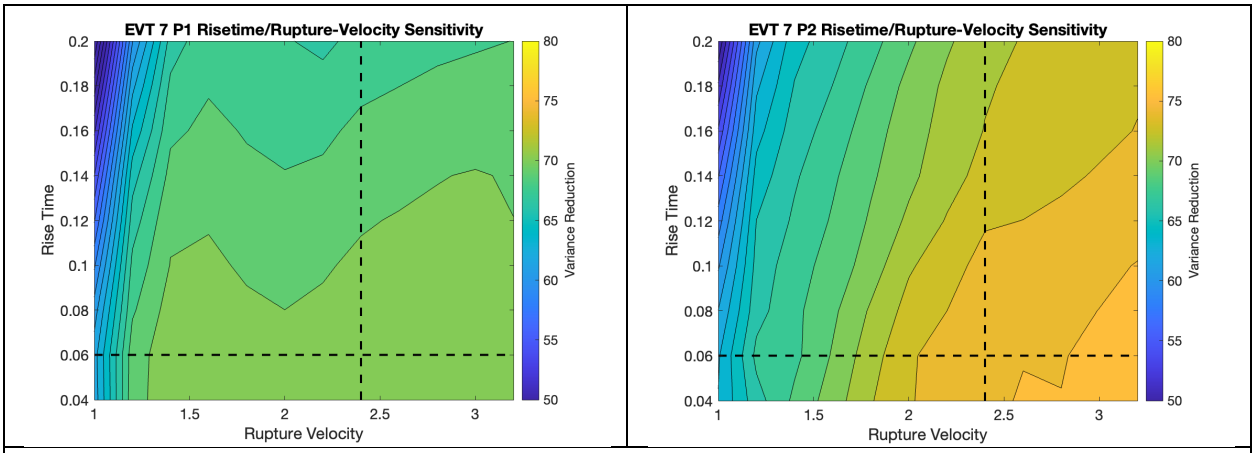

Figure 2. Rise time (seconds) and rupture velocity (km/s) sensitivity for the two moment tensor nodal planes. The color shows the fit to the data. The dashed lines show a 90% b rupture velocity, and 0.06 second rise time.

In Figure 3 the slip and stress change models are shown for plane 2 and the above values of the risetime and rupture velocity. The slip is found to a relatively simple single asperity with a slight northwestward directivity. The peak and average slip are 4.9 cm and 1.4 cm respectively, and the rupture area is 5.3 sq. km. The average and peak stress drop was found to be 0.36 and 1.46 MPa, respectively.

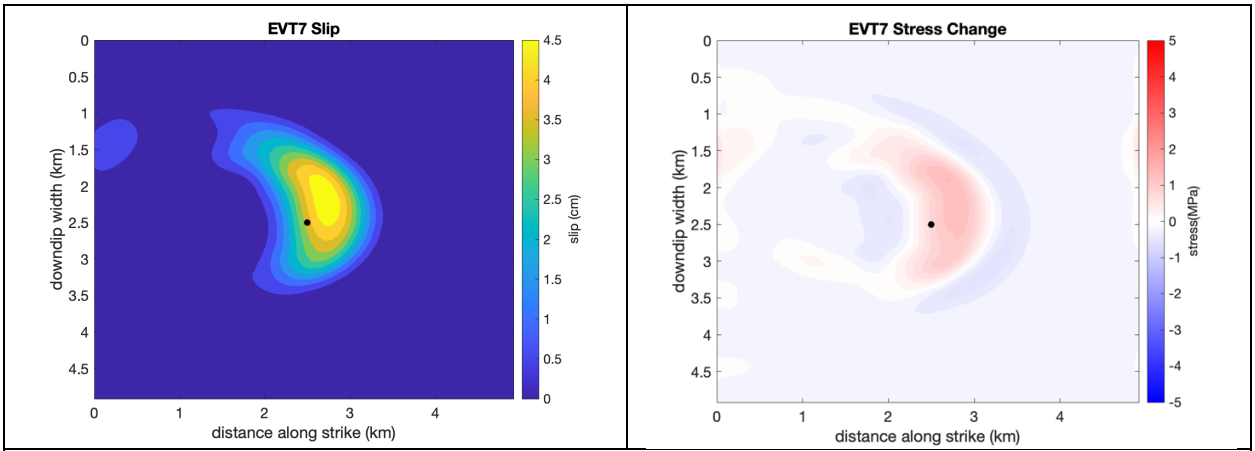

Figure 3. Slip and stress change for EVT7, Mw4.08 07/10 2019. In the stress change plot red indicates stress drop and blue stress increase. The hypocenter is shown as a black circle.

The finite-source method does require smoothing, which is essentially a free parameter in the model. We find a preferred smoothing parameter by using a tradeoff curve (Figure 4). In Figure 4 the inverse of the fit is plotted against the inverse of smoothing. An evenly logarithmic-spaced array of smoothing values was considered. The black square shows the preferred value and the circles approximately a factor of two smaller and larger. If we consider the shear wave velocity at the source depth (2700 m/s) and the average duration of 0.6 seconds effective wavelength is 1620 m. We would therefore not want to have a model whose smoothing produces features smaller than say a ¼ wavelength of approximately 400m. As shown in Figure 3 the chosen

smoothing produces a model that is consistent with the predominant wavelength in the data. We considered the values of average slip, rupture area and stress drop for the models with smoothing a factor of two smaller and larger than the preferred (circles in Figure 4) and found that one standard deviation represents 20%, 21% and 27% of the means of the respective parameters. Considering that the average stress drop is inversely proportional to the rupture area to the 3/2 power the 21% uncertainty in rupture area for the three smoothing values propagates to a 30% uncertainty in average stress drop.

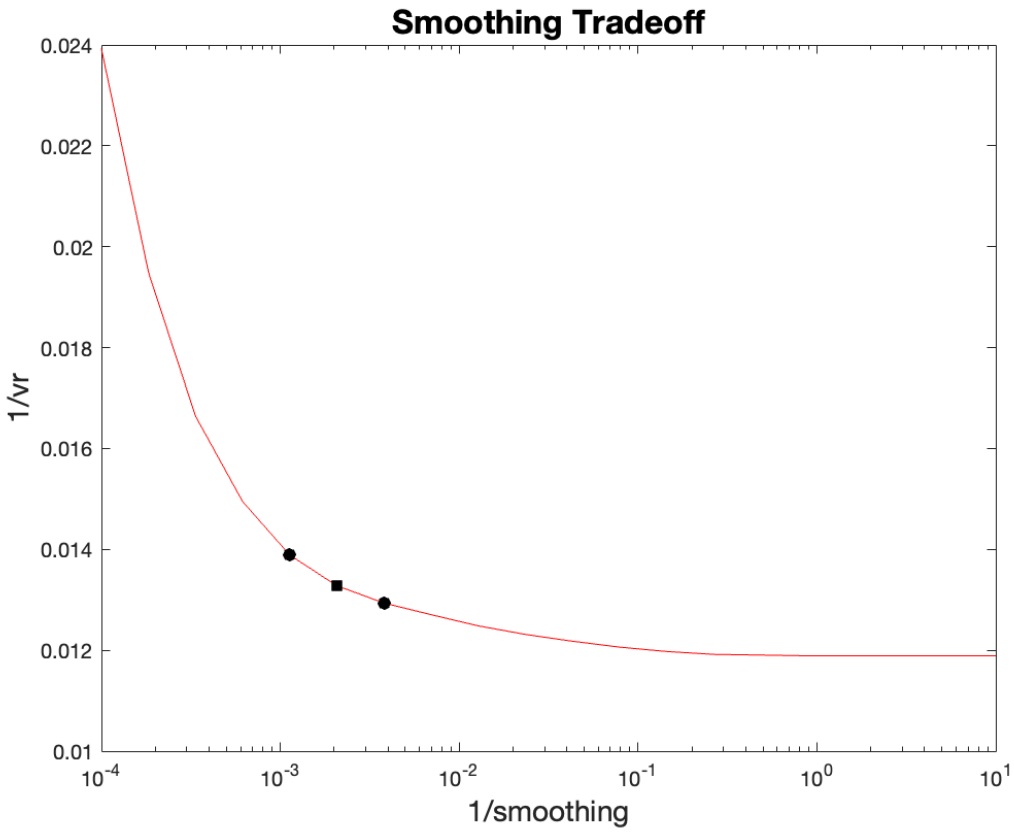

Figure 4. Inverse fit (1/vr) plotted against inverse smoothing. The black square shows the preferred model, and the black circles approximately a factor of two smaller and larger.

Fault Orientation Grid Search

For the seven studied events there are well constrained moment tensor solutions which are used as prior constraint in the finite-source inversion. We tested both nodal planes for EVT7 and found the best fitting nodal plane, or likely rupture plane as illustrated in Figure 2. Table 1 lists the preferred nodal planes for each of the 7 studied aftershocks.

As shown by Mori (1993) the EGF finite-source inverse approach can be used to find the rupture plane. We performed a grid search (10-degree steps) over fault orientation to evaluate the ability to resolve fault orientation for Ridgecrest aftershocks. We found that in most cases (events 2-7) the grid search results, as shown in Figure 5 for EVT7 found a best fitting orientation consistent with one of the nodal planes. This positive result indicates that if moment rate functions can be

obtained for smaller earthquakes that may not have well constrained focal mechanisms the finite-source method may still be reliably applied. The results for EVT1 where the grid search indicated a different solution are discussed at the end of this section.

Table 1: Fault orientation

Event	Mw	Strike (pref./conj.)	Dip (pref./conj.)	Rake[1] (pref./conj.)	Fit (pref./conj.)
EVT1*	5.53	243 / 339 / 280	66 / 76 / 80	-15 / -155 / -	64 / 56 / 68
EVT2	4.94	348 / 243	63 / 62	-148 / -31	81 / 81
EVT3	5.37	217/ 313	69 / 75	-16 / -159	87 / 77
EVT4	4.58	323 / 56	78 / 77	167 / 12	68 / 62
EVT5	4.44	127 / 20	66 / 58	-145 / -29	68 / 66
EVT6	4.09	178/ 31	59 / 31	-109 / -62	69 / 65
EVT7	4.08	323 / 232	89 / 83	-173 / -1	77 / 71

* The moment tensor fault planes did not fit well, and the grid search results (third value) are preferred.

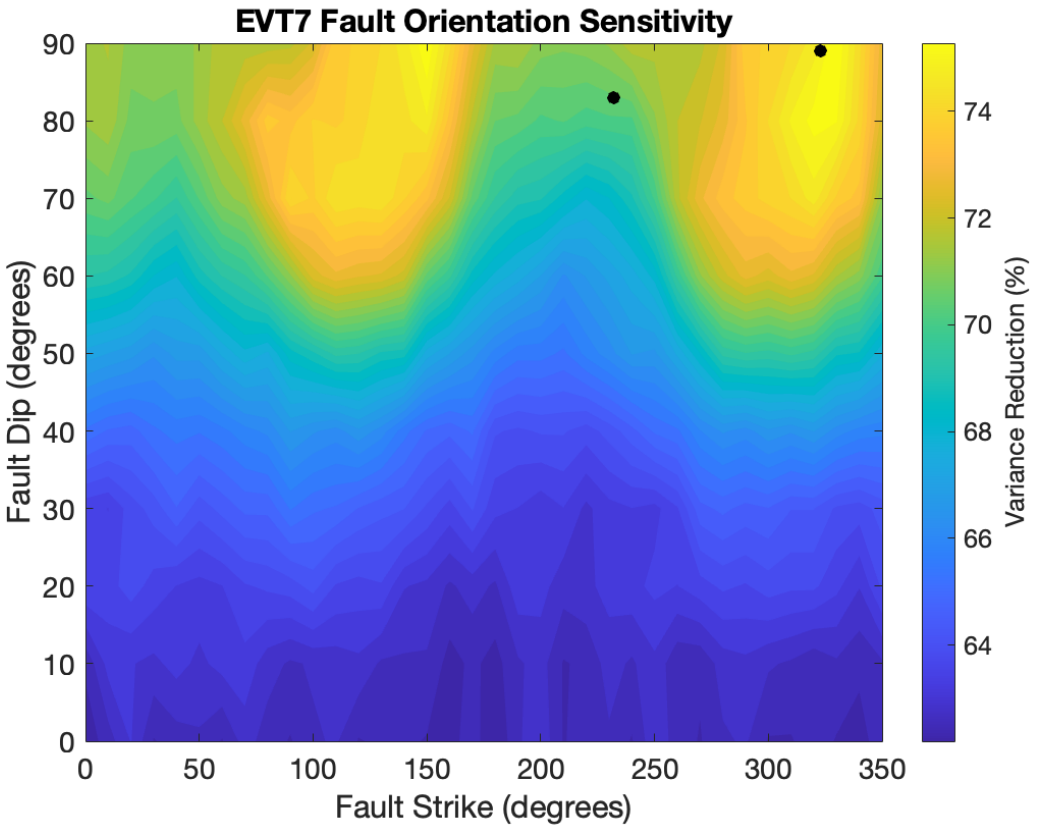

Figure 5. Fault orientation sensitivity for EVT7. Color shows data fit for all combinations of strike and dip. The black circles show the nodal planes from the moment tensor solution. Plane 2 best satisfies the data.

Considering all of the solutions in Figure 5 that fit greater 95% of the maximum fit the distributions of average slip and average rupture area may be determined. The histograms in Figure 6 show the distributions of average slip and rupture area from the >95% fit solutions. From the distributions the average and 2-sigma (assuming a gaussian distribution) are calculated. Table 2 lists the values obtained for the best fitting nodal plane solution and the fault orientation grid search results. The results indicate that it is possible to utilize a finite-source method to determine the fault orientation, average slip, rupture area and stress drop. The stress drops in Table 2 for the best nodal plane solution are calculated from the finite-source stress change calculation (e.g. Figure 3), whereas for the fault orientation grid search results the average stress drop was determined from the average rupture area using the circular fault model;

$$\Delta\sigma = \frac{7\pi^{3/2}}{16A^{3/2}} M_0.$$

The stress drops calculated for the best nodal (fault) plane solution and orientation grid search results are comparable.

Table 2: Estimated Source Parameters

		Best Fitting Nodal Plane Solution					Fault Orientation Grid Search		
Event	M_W	RT (sec)	RV (km/s)	Slip (cm)	Area(km^2)	Sd (MPa) Ave/Peak	*Slip(cm)	*Area(km^2)	Sd (MPa) Ave.
EVT1	5.53	0.06	3.6	129/41.4	13.4	17.0/77.0	51.5/21.3	10.8/4.22	17.1
EVT2	4.94	0.06	3.0	14.6/4.08	21.2	1.37/5.21	4.47/0.78	19.8/3.97	0.61
EVT3	5.37	0.04	3.2	32.5/10.0	34.1	2.85/10.9	11.6/3.04	29.6/7.55	2.17
EVT4	4.58	0.04	3.0	16.1/4.74	5.99	1.82/9.35	5.31/1.66	5.42/1.96	1.8
EVT5	4.44	0.04	3.0	19.4/3.95	4.92	2.31/15.5	5.40/1.30	3.19/0.89	2.46
EVT6	4.09	0.06	2.0	16.50/5.43	1.48	2.35/7.88	5.87/0.99	1.34/0.31	2.70
EVT7	4.08	0.06	2.4	4.86/1.44	5.30	0.36/1.46	1.47/0.27	5.35/1.15	0.33

RT is risetime (sec), and RV is rupture velocity (km/s). * mean and 2-sigma uncertainty are given.

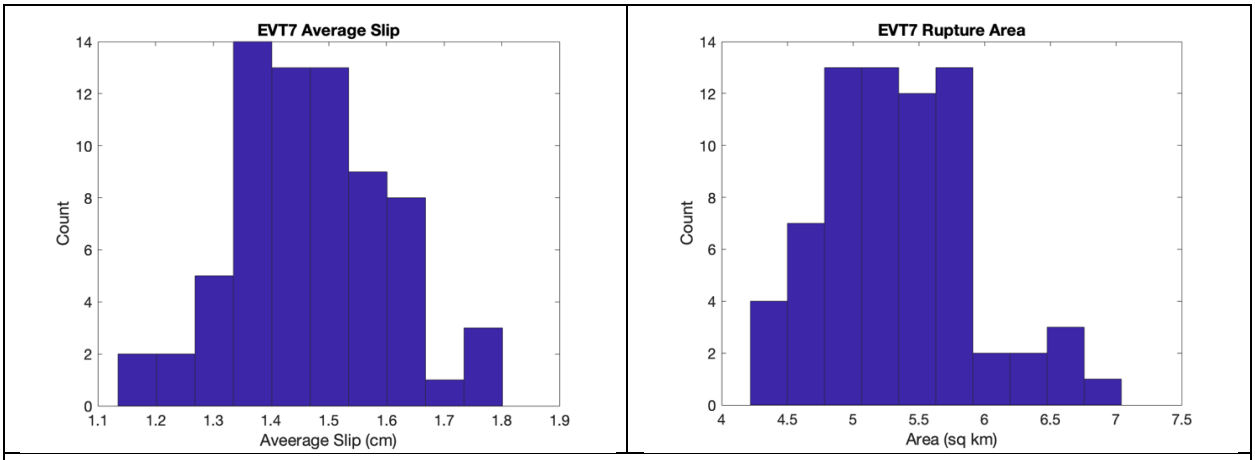

Figure 6. Distribution of solutions for EVT7 that fit better than 95% of the best fit to the data. The left shows average slip of the models, and the right is the rupture area.

EVT1 was one event where neither of the nodal planes from moment tensor analysis fit the data particularly well. The grid search found that a solution that is rotated 37-degrees in strike, and 16-degrees in dip that better fit the moment rate data (Figure 7). Table 2 shows that the average stress drop for the grid search results is nearly the same as the best nodal plane solution, and is the highest of the events studied so far (~17MPa). This event was also the largest earthquake (Mw 5.53) and it is possible that the actual rupture was more complex than allowed by the model (non-planar, or multiple plane rupture). Nevertheless, the fault orientation grid search results indicate that stress drop maybe determined from EGF finite-source inversions may be determined even in cases where an a priori fault orientation is unknown.

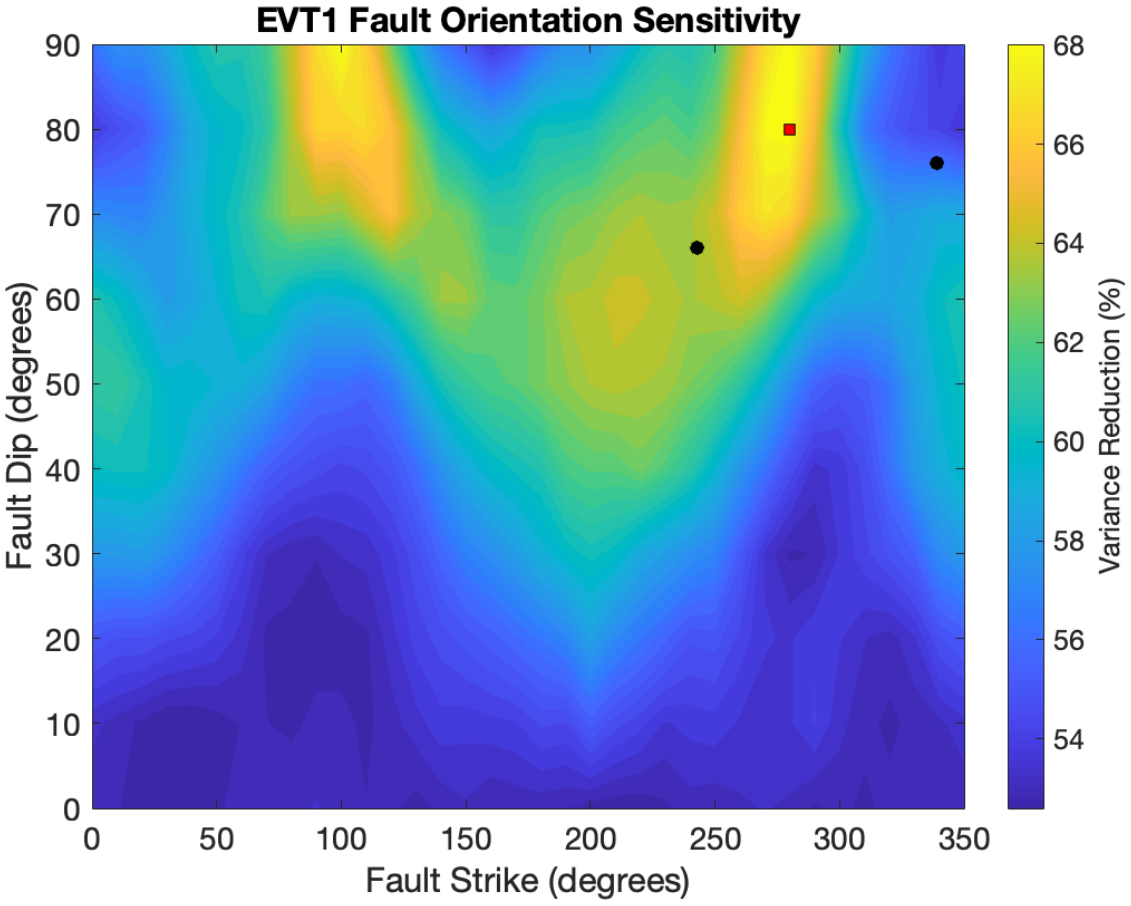

Figure 7. Mechanism sensitivity for EVT1. The two black circles show the moment tensor nodal planes, and the red square shows the best solution from the fault orientation search.

Earthquake Scaling and Stress Drop

Rupture area and average slip for the best fitting nodal plane solution are plotted in Figures 8 and 9, respectively. The Leonard (2010) scaling laws for strike-slip earthquakes are shown as red lines, and the two standard deviation uncertainty is plotted as red dotted lines. The estimated rupture area for the events ranging in magnitude from 4.0 to 7.0 (Figure 8) are found to agree well with Leonard (2010) scaling within the 2-sigma uncertainty. EVT7 lies just outside the 2-

sigma ranges and has a substantially larger rupture area indicating a lower stress drop (0.36MPa). The gray lines show stress drop for 0.1, 1.0, 10 and 100. MPa. The average slip (Figure 9) also compares with Leonard (2010) well withing the 2-sigma uncertainty level. On average the events appear to have a stress drop a little lower than implied by Leonard (2010) scaling and is in the range of 1-3 MPa. A regression of log rupture area to log moment yields a slope of 0.57 (R^2=0.93) compared to the self-similar value of 0.67 suggesting ruptures become slightly more compact for increasing moment, however a regression of stress drop with moment indicates a scaling of ~$M_0^{0.1}$ with an insignificant R^2 of 0.18.

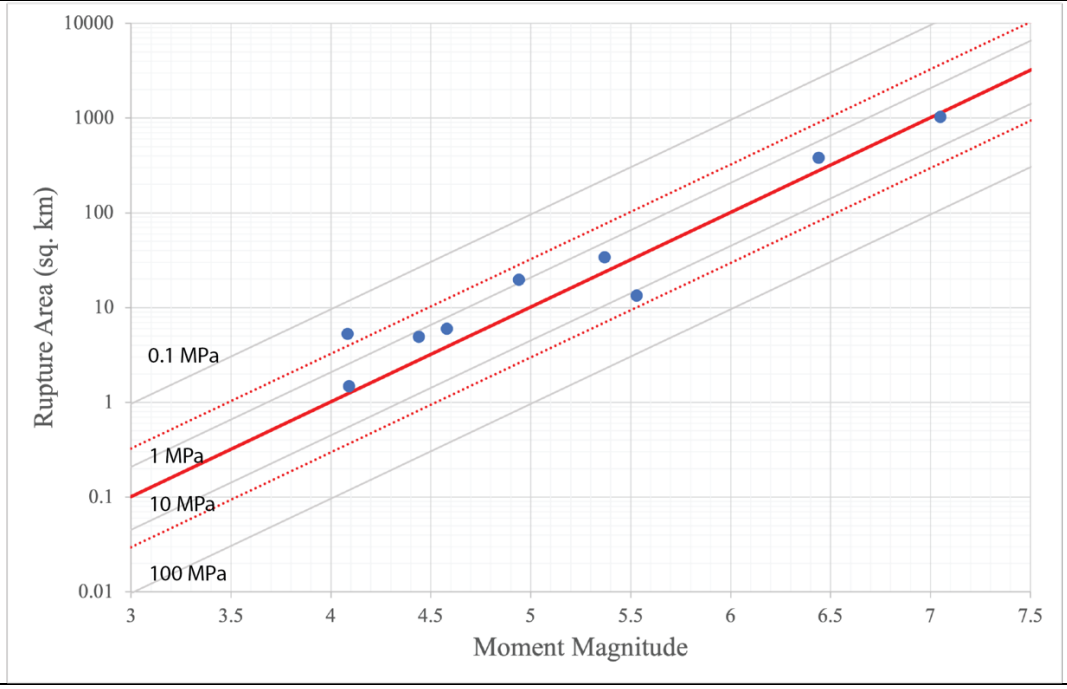

Figure 8. Rupture area from the finite-source inversion is compared to the Leonard (2010) scaling law (red line; dotted red lines are 2-sigma uncertainty). The gray lines show stress drop.

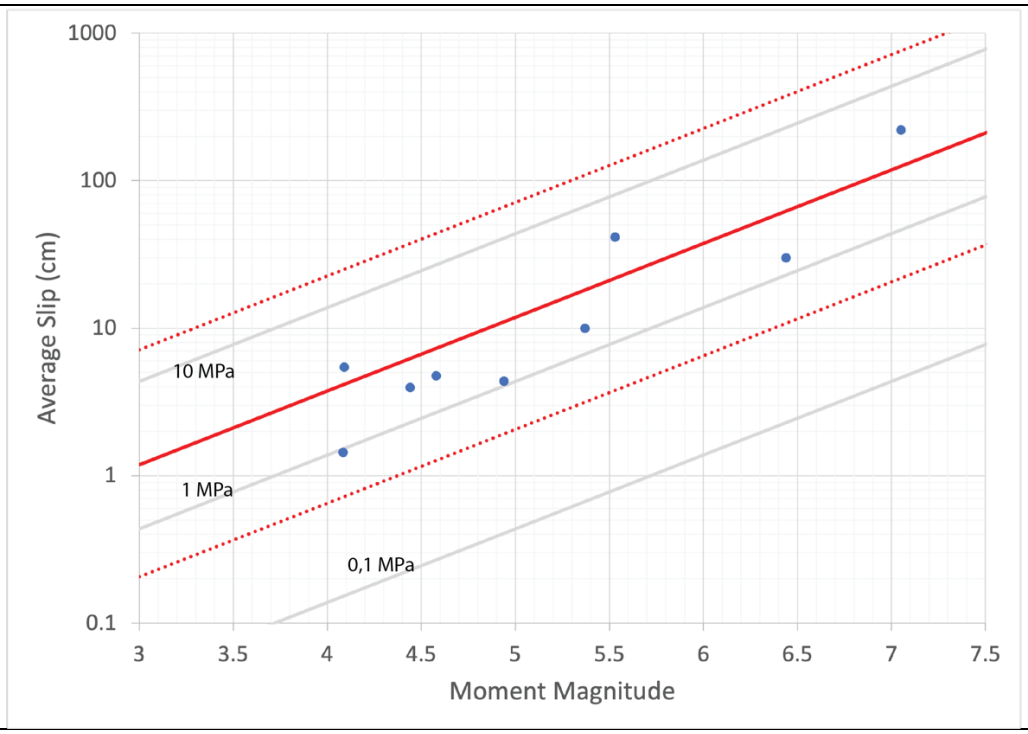

Figure 9. Average slip from the finite-source inversions is plotted against the Leonard (2010) scaling law (red line; dotted red lines are 2-sigma uncertainty). The gray lines show stress drop.

Automated Rupture Duration and Scaling

The durations of the estimated MRF for 67 Ridgecrest earthquakes (3.27 <= M <= 5.44) are computed by measuring the time from the first zero-crossing to a second zero-crossing of the primary MRF pulse. For each target Ridgecrest earthquake, possible EGF events were selected; if events had 1) at least one magnitude unit smaller and 2) located within 5 km horizontally and 2 km vertically from target events. MRFs of target events were determined by a frequency-domain water level deconvolution (Clayton and Wiggins, 1976). A water level of 1% was used to stabilize the deconvolution procedure. We performed the deconvolution separately for each component and then stacked the three-component MRFs at each station. The quality of resultant MRFs were evaluated based on signal-to-noise ratio (SNR). If SNR exceeds 10, the measured MRF durations were used for further analysis. This same measurement criteria was used in the finite-source method to have a consistent measurement for all event-station combinations, and to avoid errors due to (acausal) side lobes in the spectral deconvolution MRF functions. The procedure may be automated enabling the bulk processing of many events. As Figure 10 shows there is scatter in the measurements for a given event (magnitude), which is likely due to the unaccounted rupture directivity, however the plot shows a systematic increase in duration with magnitude that is consistent with self-similar scaling for a stress drop of 2MPa.

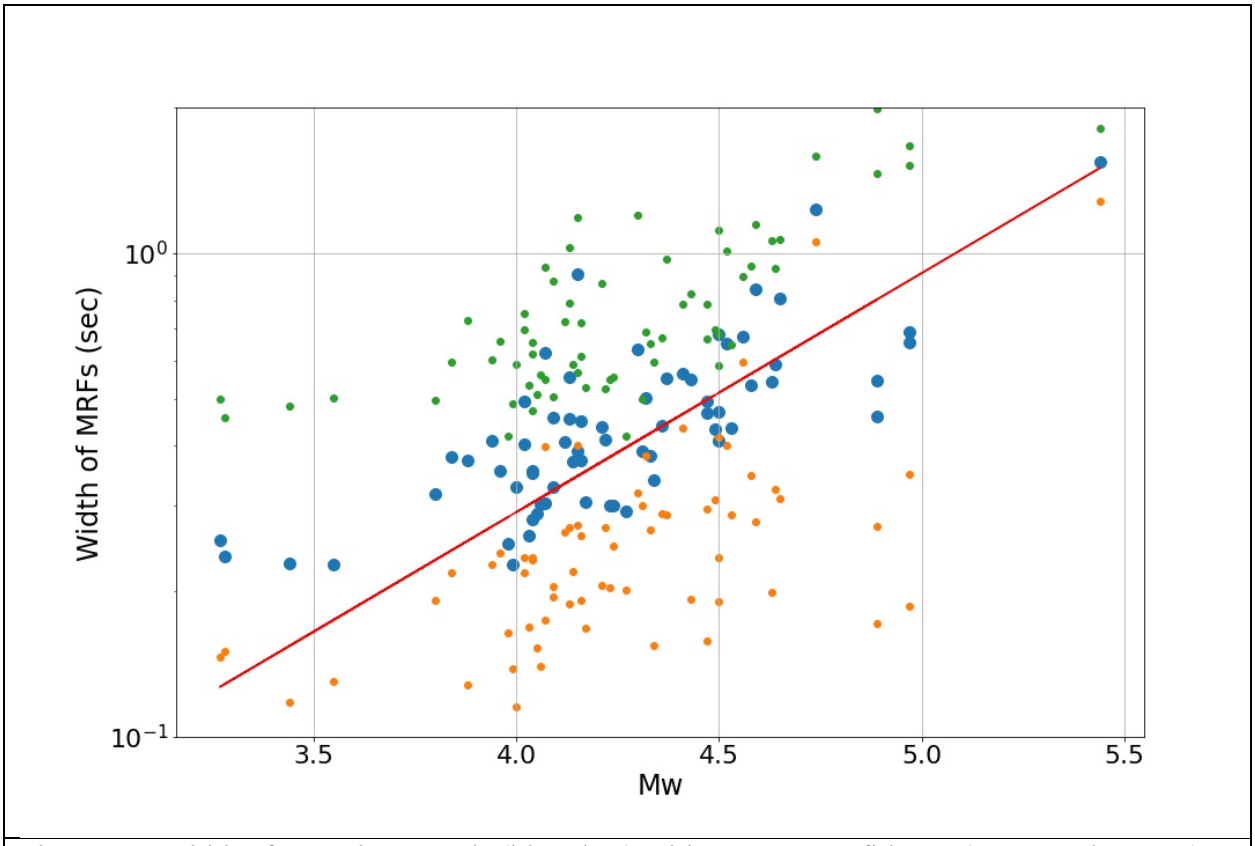

Figure 10. Width of MRF in seconds (blue dots) with +- 95% confidence (green and orange). The red line shows circular fault model scaling assuming a stress drop of 2 Mpa.

Conclusions

The applied finite-source inverse method to determine earthquake source scaling and stress drop accounts for possible variability due to focal mechanism, and rupture directivity. The effects of path structure and site effects are effectively removed by using moment rate functions obtained through empirical Green's function deconvolution. For the 9 earthquakes considered, ranging in magnitude from 4.0 to 7.0 we find that although there is a slight suggestion of $\sim M_0^{0.1}$ scaling of stress drop with moment it is not statistically significant and the events studied are to first order self-similar, and consistent with the Leonard (2010) relationship. On average the stress drop is between 1-3 Mpa, though low and high stress drop outliers are observed. Continuing work is investigating finite-source solutions for more Ridgecrest aftershocks.

References

Antolik, M., D. Dreger, and B. Romanowicz (1996), Finite Fault Source Study of the Great 1994 Deep Bolivia Earthquake, Geophys Res. Lett., 23, 1589-1592.

Antolik, M., A. Kaverina, and D. Dreger (2000). Compound rupture of the great 1998 Antarctic Plate earthquake, J. Geophys. Res., V105, 23,825-23,838.

Brune, J.N. (1970). Tectonic stress and the spectra of seismic shear waves from earthquakes, J. geophys. Res., 75, 4997–5009.

Clayton, R. W., and R. A. Wiggins, 1976, Source shape estimation and deconvolution of teleseismic body waves, Geophys. J. Int., 47, no. 1, 151–177, doi: 10.1111/j.1365-246X.1976.tb01267.x.

Dreger, D., R. Nadeau, and A. Chung (2007), Repeating Earthquake Finite-Source Models: Strong Asperities Revealed on the San Andreas Fault, *Geophys. Res. Lett.,* 34, L23302, doi:10.1029/2007GL031353.

Dreger, D. (1997), The Large Aftershocks of the Northridge Earthquake and their Relationship to Mainshock Slip and Fault Zone Complexity, Bull. Seism. Soc. Am., 87, 1259-1266.

Dreger, D. S. (1994), Investigation of the Rupture Process of the 28 June 1992 Landers Earthquake Utilizing TERRAscope, Bull. Seism. Soc. Am., 84, 713-724.

Hartzell, S. (1978). Earthquake aftershocks as Green's functions, Geophys. Res. Lett., Vol. 5, pp. 1-4.

Heaton, T. H. (1990). Evidence for and implications of self-healing slip pulses of slip in earthquake rupture, Phys. Earth Planet Int., 64, 1, 1-20.

Hough, S. E., D. S. Dreger (1994), Source Parameters of the 4/22/92 M6.1 Joshua Tree, California Earthquake and its Aftershocks: Empirical Green's Function Analysis of GEOS and TERRAscope Data, Bull. Seism. Soc. Am., 85, 1576-1590.

Kaneko, Y., P. M. Shearer (2014). Seismic source spectra and estimated stress drop derived from cohesive zone models of circular subshear rupture, Geophys. J. Int., 197, 1002-1015, doi: 10.1093/gji/ggu030

Leonard, M. (2010). Earthquake fault scaling: Self-consistent relating of rupture length, width, average displacement, and moment release, Bull. Seism. Soc. Am., 100, 5A, 1971-1988, doi: 10.1785/0120090189.

Madariaga, R. (1976). Dynamics of an expanding circular fault, Bull. seism. Soc. Am., 66(3), 639–666.

Mori, J., and S. Hartzell (1990). Source inversion of the 1988 Upland, California earthquake: Determination of a fault plane for a small event, Bull. Seism. Soc. Am., 80, 507-518.

Mori, J. (1993). Fault plane determinations for three small earthquakes along the San Jacinto fault: Search for cross faults, J. Geophys. Res., 98, B10, 17,711-17,722.

Ripperger, J., and P. M. Mai (2004), Fast computation of static stress changes on 2D faults from final slip distributions, *Geophys. Res. Lett.*, *31*, L18610, doi:10.1029/2004GL020594.

Sato, T. & Hirasawa, T. (1973). Body wave spectra from propagating shear cracks, J. Phys. Earth, 21, 415–431.

Wang, K., D. S. Dreger, E. Tinti, R. Bürgmann, and T. Taira (2020). Rupture Process of the 2019 Ridgecrest, California Mw 6.4 Foreshock and Mw 7.1 Earthquake Constrained by Seismic and Geodetic Data, Bull. Seismol. Soc. Am. 110(4), 1603–1626 , doi: 10.1785/0120200108